PNAS RESEARCH ARTICLE | MEDICAL SCIENCES

Magnetically actuated microrobotic system for sequential treatment of biofilm

Shunyao Li[a,1], Yu Mei[b,c,1], Kai Xu[a,1], Huaixuan Sheng[a], Yu-an Chen[b], Mingda Teng[d], Bohan Xu[a], Bingqian Jiang[a], Chengxuan Yu[a], Huizhu Li[a], Shiyun Zhao[b,c], Yi Wang[b], Xiao Zhang[a], Yiyang Zhao[e], Yueming Wang[f], Yan Wo[f], Zhaochen Li[g], Siwen Shen[h], Yunxia Li[a], Min Tang[e], Yongfeng Mei[c,i,j,2], Jun Chen[a,2], Gaoshan Huang[b,c,2], and Sijia Feng[a,2]

Affiliations are included on p. 10.

Edited by Wei Gao, California Institute of Technology, Pasadena, CA; received December 11, 2025; accepted May 26, 2026 by Editorial Board Member Scott J. Hultgren

Biofilm-associated infections present a critical therapeutic challenge due to antibiotic resistance and impaired tissue healing. Here, we present a microrobotic system (MZ-8) that integrates real-time human-steered navigation with autonomous, microenvironment-responsive therapy to actively eradicate biofilms and promote tissue regeneration. This microrobotic system features a spine-inspired structure for mechanical biofilm disruption, a pH-responsive ZIF-8 coating for immunomodulatory Zn^{2+} release, and closed-loop actuation under second near-infrared fluorescence guidance. In a rat model of periprosthetic joint infection, MZ-8 achieved effective biofilm removal, induced a pro-regenerative immune response by polarizing macrophages toward the M2 phenotype, and significantly enhanced tissue regeneration. Transcriptomic analysis further revealed the activation of immunomodulatory pathways and upregulation of M2-associated genes, confirming the system's sequential shift from eradication to repair. Moreover, validation in a rabbit model and human knee joint confirmed its operational feasibility under clinical imaging guidance and excellent biosafety. This work establishes that integrating physical eradication, biochemical immunomodulation, and interactive control within a single system is essential for advancing from infection clearance to functional tissue restoration. Thus, it provides a therapeutic paradigm for biofilm-associated diseases and lays a foundation for future intelligent, clinically adaptive anti-infective systems.

biofilm-associated infections | micro/nanorobotics | sequential treatment

Significance

Biofilm's physical matrix impedes its eradication, and even after removal, the local immune microenvironment remains impaired, preventing tissue repair. Here we present a magnetically actuated microrobotic system for sequential treatment of biofilm. In this system, microrobots' biomimetic spiny surface mechanically disrupts the biofilm under real-time second near-infrared fluorescence imaging guidance, and its Zeolitic imidazolate framework-8 coating releases zinc ions in response to the acidic infection microenvironment to promote immunomodulation and tissue repair. This strategy is validated in rat and rabbit models and further translated to a human knee joint. Beyond this specific system, the concept of sequential eradication and immunomodulation offers a framework for the design of microrobots for infectious diseases.

Modern infection management has long focused on pathogen eradication (1–3), often overlooking the biological aftermath left in its wake. Antibiotics, debridement, and antiseptics can effectively suppress infection, yet the surrounding tissue frequently remains ischemic, inflamed, and immunologically exhausted (4, 5). Treating eradication as cure has therefore hindered progress against biofilm-associated diseases, exemplified most notably by periprosthetic joint infections (PJI) (6). These resilient bacterial communities, encased within extracellular polymeric substances (EPS), form not only a physical barrier that shelters persisted cells from antibiotics but also a metabolically active "pathological organ" that sabotages local vasculature, stem-cell niches, and immune homeostasis (6–8). Conventional strategies—systemic antibiotics combined with surgical debridement—focus solely on source control and often succeed only in extinguishing infection while leaving behind a biologically depleted landscape. Consequently, recurrence and nonunion persist as common outcomes (6). Thus, PJI demands more than eradication: it requires an integrated therapeutic logic that couples robust biofilm eradication with active tissue repair, transforming infection control from a one-act treatment into a full symphony of restoration.

Microrobots, defined as miniaturized devices capable of active motion and task execution under human control, embody the required shift from mere pathogen eradication to combined clearance and functional restoration (9, 10). On one hand, they can perform as potent biofilm eradicators by penetrating the EPS matrix and achieving localized killing (11–13). On the other hand, they can act as targeted delivery platforms for immunomodulators and pro-regenerative factors (14–16). This dual functionality directly mitigates the risk of leaving a biologically barren microenvironment, uniting both therapeutic goals within a single, minimally invasive platform. However, prior efforts have typically pursued these capabilities in isolation—some microrobots that mechanically disrupt biofilms or deliver bactericidal agents (11–13, 17), while others focus on platforms designed to promote tissue regeneration (15, 16). Hence, an integrated paradigm that unites both

The authors declare no competing interest.

This article is a PNAS Direct Submission. W.G. is a guest editor invited by the Editorial Board.

[1]S.L., Y.M., and K.X. contributed equally to this work.

[2]To whom correspondence may be addressed. Email: yfm@fudan.edu.cn, biochenjun@fudan.edu.cn, gshuang@fudan.edu.cn, or sjfeng13@fudan.edu.cn.

This article contains supporting information online at https://www.pnas.org/lookup/suppl/doi:10.1073/pnas.2535216123/-/DCSupplemental.

Published July 6, 2026.

eradication and repair within a single system has yet to be realized. Additionally, most antibiofilm microrobots remain confined to in vitro demonstrations, with limited evidence of their efficacy in vivo (18). The true potential of microrobots, however, lies not merely in multifunctional design but in their capacity to serve as interactive therapeutic executors (10, 19), capable of dynamically coupling pathogen clearance with repair-promoting interventions under external control. Yet such multifunctionally integrated, imaging-guided microrobotic systems remain exceedingly rare, underscoring the need for a new class of biofilm-adapted microrobots that can embody this therapeutic duality in vivo (18, 20).

Here, we report a bioinspired sequential microrobotic system, MZ-8, derived from natural pollen grains (PGs) and functionalized with Fe_3O_4 nanoparticles and a Zeolitic Imidazolate Framework-8 (ZIF-8) coating, which combines biomimetic morphology, magnetic control, and biofilm microenvironment-responsive zinc ions (Zn^{2+}) release. Under magnetic guidance, it exhibits swarm-like locomotion through confined spaces and triggers Zn^{2+} release in acidic environments. In vitro, MZ-8 efficiently eradicates biofilms under different circumstances and successfully induces M2 macrophage polarization. In a PJI animal model, its magnetically controllable locomotion, coupled with real-time in vivo imaging, enables precise navigation and active biofilm eradication, while its biofilm-triggered Zn^{2+} release provides sequential immunomodulation to repair damaged tissues. Preclinical studies in rabbit models and human knee specimens further validate its controllability and translational potential. In brief, MZ-8 integrates spatiotemporally controlled biofilm eradication with sequential immunomodulation in a single platform. This "scrape-and-supply" strategy represents a technological breakthrough that establishes a clinically translatable paradigm for tackling biofilm-associated infections and their downstream tissue repair.

Results

Design and Functional Integration of the Microrobotic System. Biofilm-associated infections are frequently exacerbated by biofilm formation on device surfaces. Encased within a cohesive EPS matrix, biofilms exhibit exceptional recalcitrance to antimicrobial clearance and elicit progressive tissue destruction. An optimal therapeutic paradigm for biofilm-associated infections necessitates a sequential, two-stage strategy: i) complete eradication of the biofilm and ii) targeted restoration of the compromised osseous microenvironment. Accordingly, a hierarchically integrated, two-stage microrobotic platform was rationally engineered in precise temporal order (Fig. 1*A*).

In nature, the spiny architecture of sea urchins facilitates the removal of surface-attached organisms, while their porous skeleton supports material exchange and movement (21–23). Inspired by the natural traits of sea urchins, a stepwise fabrication process was employed to develop the Microrobots-ZIF-8 system (MZ-8). The biomimetic process began with the PGs cluster, which was first synthesized into Fe_3O_4 nanoparticles, PGs@Fe_3O_4 (PGF). This was followed by the deposition of a conformal ZIF-8 coating around the pollen, PGF@ZIF-8, constructing the final MZ-8 structure. The as-prepared MZ-8 microrobots faithfully preserved the echinate surface architecture of PGs; concomitantly, the ZIF-8 coating imparted a biomimetic, sea urchin-inspired exoskeleton that markedly augmented both mechanical robustness and functional performance (Fig. 1*B*).

The fabricated spike-like morphology of MZ-8 enabled it to efficiently scrape biofilms, mimicking the biofilm-clearing capabilities of sea urchins (Fig. 1 *C*1 and *C*2). SEM imaging confirmed the distinct spiky surface of MZ-8 (Fig. 1*C*3), with high magnification details showing the smooth surface of PGs (*SI Appendix*, Fig. S1) transitioning to the ZIF-8 encapsulated structure of MZ-8 (Fig. 1*C*4). This transition highlights the unique structural characteristics of MZ-8, with the ZIF-8 layer forming a robust coating on the surface of the spike-like template. The magnetic responsiveness of MZ-8 was further investigated through BF imaging (Fig. 2*D*1 and *SI Appendix*, Fig. S2). Initially, MZ-8 particles settled at the bottom; after shaking, they dispersed into suspension (*SI Appendix*, Fig. S2). Under magnetic control, they adhered to the walls of the vial (Fig. 2*D*1). This behavior confirmed the ability of MZ-8 to be magnetically controlled. The magnetization curve shown in Fig. 2*D*2 revealed a saturated magnetization of 29.8 (emu) g^{-1} for MZ-8, owing to the specific material properties of MZ-8. Collectively, the results indicated that MZ-8 integrates an echinate microarchitecture with magnetically responsive actuation, possessing the ability to eradicate recalcitrant biofilms.

Furthermore, the functional porous ZIF-8 coating of MZ-8 was deciphered. First, SEM imaging was employed to examine the surface features of the ZIF-8 coating, revealing that ZIF-8 layer uniformly coats the surface of the claw-shaped template (Fig. 1*E*1). The elemental mapping confirmed the uniform distribution of elements within the MZ-8, including carbon (C) (Fig. 1*E*2), oxygen (O) (Fig. 1*E*3), iron (Fe) (Fig. 1*E*4), nitrogen (N) (Fig. 1*E*5), and zinc (Zn) (Fig. 1*E*6). The elemental mapping in the SEM results highlighted Fe, O, and Zn as key elements within the MZ-8 structure, verifying the presence of Fe_3O_4 for magnetic control and ZIF-8 as the functional coating. Then, the particle size distribution of MZ-8, which indicates that most particles have a size around 17.5 μm (Fig. 1*F*1), while the size range of PGs was observed around 25 μm (*SI Appendix*, Fig. S3). The successful formation of ZIF-8 and Fe_3O_4 was further verified by various techniques. Fourier-transform infrared spectroscopy (FTIR) confirmed Zn-N and Fe-O stretching vibrations, indicating the presence of ZIF-8 and Fe_3O_4 (*SI Appendix*, Fig. S4), while XPS revealed a prominent Zn 2p peak and XRD showed a characteristic broad peak shift around 20°, collectively verifying the successful ZIF-8 coating on MZ-8 (Fig. 1*F*2 and *SI Appendix*, Fig. S5). Thermogravimetric analysis (TGA) results (*SI Appendix*, Fig. S6) indicated excellent thermal stability, with decomposition only occurring above 270 °C.

The therapeutic workflow of MZ-8 was established as a sequential two-step strategy including movement under magnetic control and acid-responsive Zn^{2+} release. First, single MZ-8 was magnetically piloted to execute precise spinning, fixed, and rolling motions (*SI Appendix*, Fig. S7). Subsequently, a swarm of MZ-8 (100 μL) was steered through a microfluidic maze within 19 s (Fig. 1*G*), corroborating the feasibility of scalable, collective motion control for the MZ-8 platform. To simulate navigation through a biologically confined space, the MZ-8 swarm was guided through the narrow joint space (~0.5 mm in width) between the femur and tibia in a knee joint phantom (Fig. 1*H*1). The swarm exhibited stable, collective locomotion through this constricted channel (Fig. 1*H*2 and Movie S1), demonstrating precise magnetic control and maneuverability that mimics traversal of anatomical passages. Magnetic field distribution analysis further verified the sufficient gradients for stable swarm manipulation inside the joint phantom (*SI Appendix*, Fig. S8). In brief, these data establish the scalability of MZ-8 swarm navigation from simple pathways to complex, three-dimensional anatomical topographies, evidencing a progressive enhancement in navigational complexity while maintaining positional accuracy.

For functional purpose, the ZIF-8 coating of MZ-8 was fabricated to display pronounced pH-responsiveness, with Zn^{2+} release

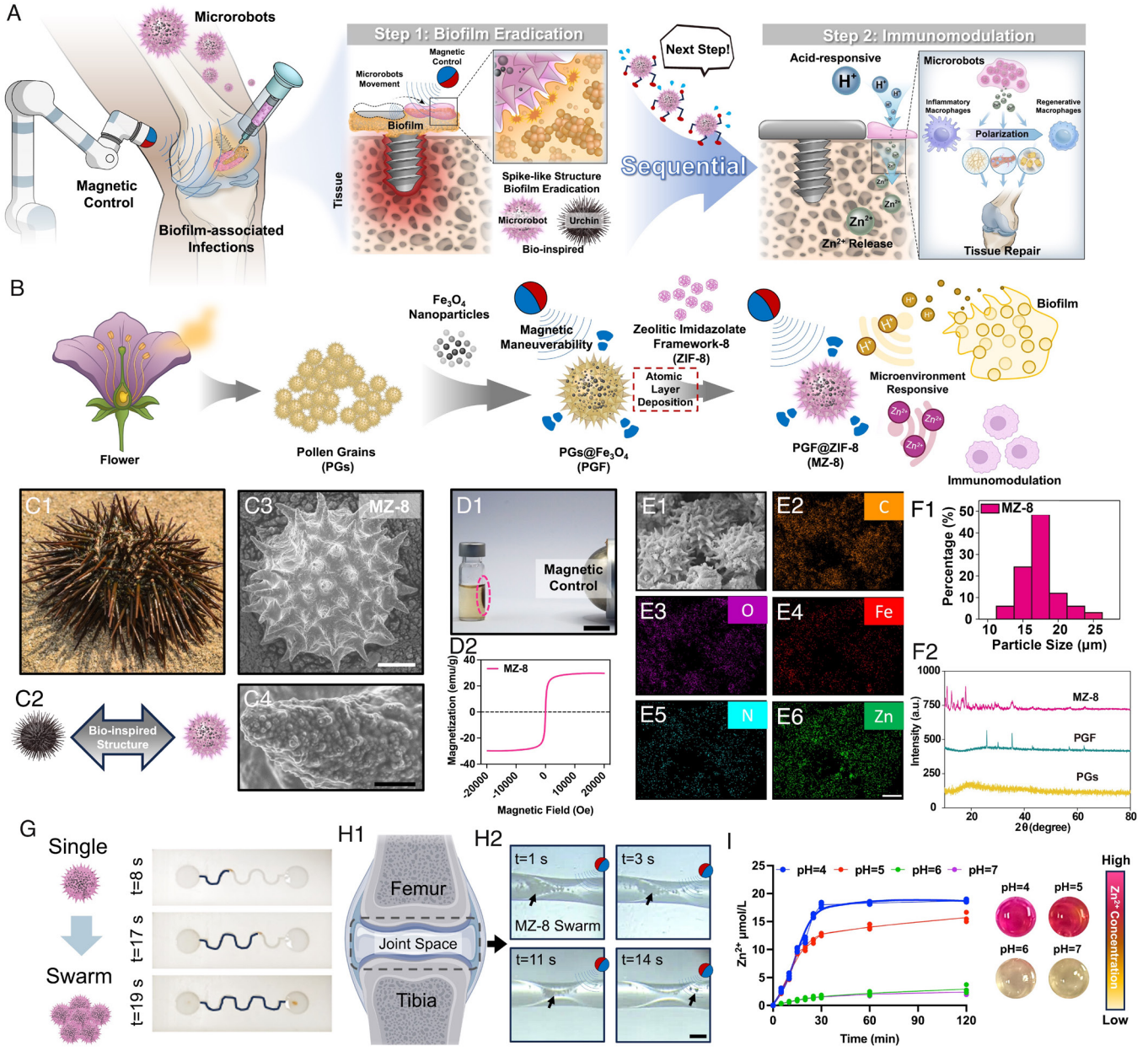

Fig. 1. Design and Functional Integration of the Microrobotic System. (*A*) Schematic illustration of MZ-8 mediated biofilm eradication and regenerative immunomodulation. (*B*) Fabrication process and functional evolution of the bioinspired MZ-8. (*C1* and *C2*) Images of urchin and the bioinspired design of MZ-8. Scanning electron microscopy (SEM) images showing the spike-like morphology of MZ-8 (*C3*) (Scale bar, 5 μm.), with high magnification details (*C4*) (Scale bar, 500 nm.) Bright-field (BF) image of magnetic control of MZ-8 (*D1*) (Scale bar, 1.5 cm.) (*D2*) Magnetic hysteresis loop. (*E1*) SEM images of the ZIF-8 surface structure and elemental mapping of MZ-8 indicating the distribution of C, O, Fe, N, and Zn (*E2*–*E6*). (*F1*) Particle size distribution of MZ-8. (*F2*) Structural characterizations of MZ-8 using XPS. (*G*) Schematic and BF images of locomotion modes of a swarm of MZ-8 navigating through a microfluidic maze. (*H1*) Schematic illustration of the knee joint phantom. (*H2*) MZ-8's swarm movement within a knee joint phantom under magnetic control. (indicated by black arrows) (Scale bar, 1 mm.) (*H1*) is adapted from figure created in BioRender. H. Lee (2026) https://BioRender.com/kor84sm. (*I*) Time-dependent Zn^{2+} release from MZ-8 at varying pH levels and representative BF images of Zn^{2+} concentration of MZ-8.

significantly accelerated under acidic microenvironment. Time-resolved release assays showed that at pH 4.0 to 5.0, Zn^{2+} release increased gradually within the first 30 min and then reached a sustained plateau, whereas release remained minimal at pH 6.0 to 7.0 (Fig. 1*I* and *SI Appendix*, Fig. S9), indicating that MZ-8 selectively accelerates Zn^{2+} release within the acidic milieu characteristic of biofilm. Conversely, MZ-8 exhibited excellent stability under neutral to alkaline conditions, with almost no detectable degradation (*SI Appendix*, Fig. S10). This temporal profile aligns with a sequential therapeutic requirement—minimal Zn^{2+} exposure during the early eradication phase of biofilm, followed by a suprathreshold concentration available at the onset of subsequent tissue repair process. Taken together, the findings demonstrate that the MZ-8 microrobotic system synergized a biomimetic spiky morphology for mechanical biofilm disruption, magnetic maneuverability for guided navigation, and a pH-responsive ZIF-8 coating for on-demand Zn^{2+} release, executing a sequential two-stage strategy for biofilm eradication and subsequent tissue repair.

In Vitro Antibacterial Activity and Immunoregulatory Effects of MZ-8. The antibiofilm activity of MZ-8 swarm was evaluated in vitro. In accordance with the sequential treatment strategy, the first stage involved magnetic swarm-mediated biofilm eradication. Under magnetic control, MZ-8 swarm executed controlled

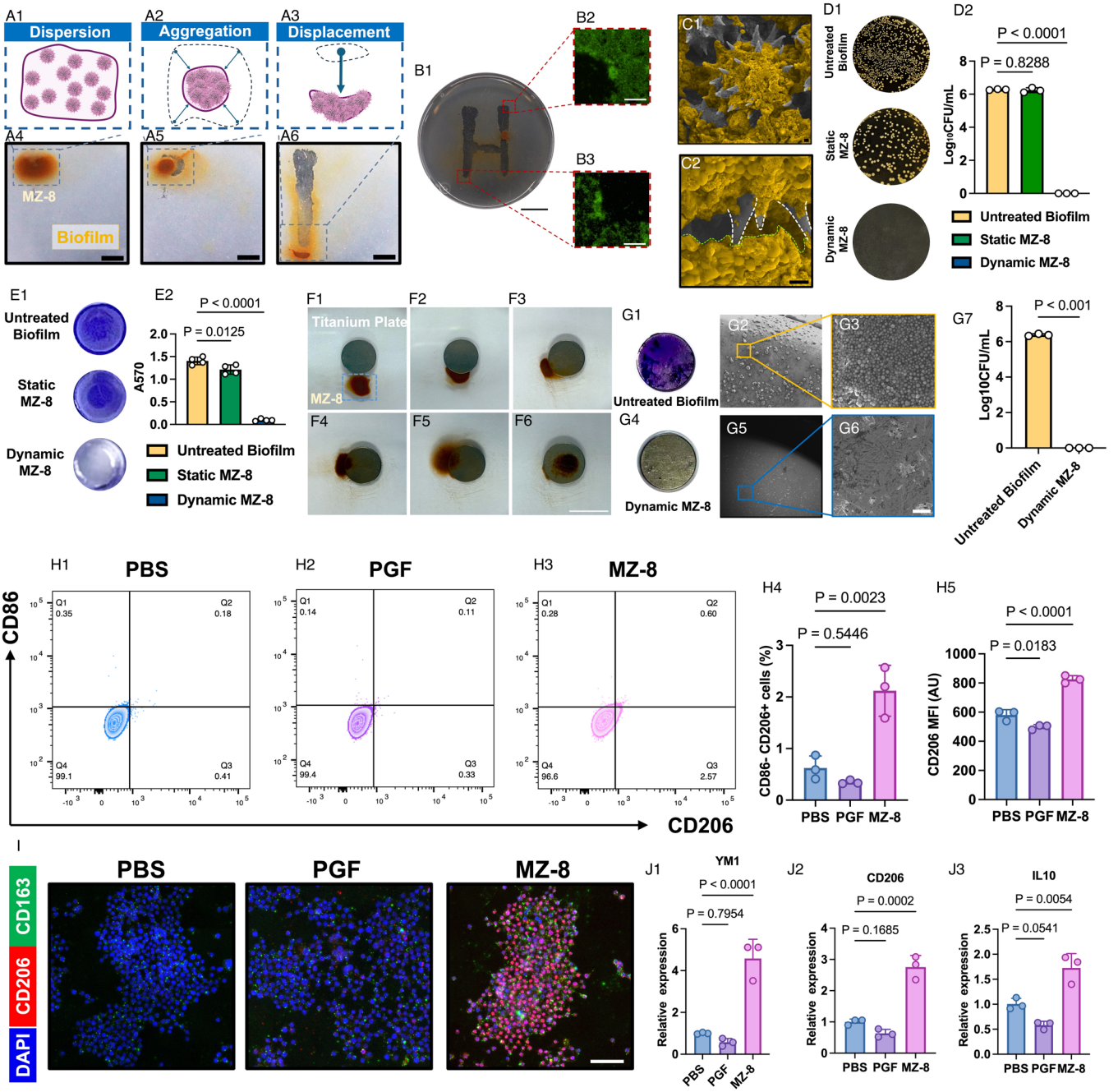

Fig. 2. In vitro antibiofilm activity and immunoregulatory effects of MZ-8. (*A1–A3*) Schematics of MZ-8 swarm's biofilm eradication on culture dishes including: Dispersion, Aggregation, and Displacement behaviors; (*A4–A6*) representative BF images showing corresponding MZ-8 swarm's behaviors. (Scale bar, 2 cm.) (*B1–B3*) Biofilm eradication on agar plates, with corresponding fluorescence staining results. [black (Scale bar, 2 cm.); white (Scale bar, 0.5 mm.)] (*C1*) SEM image of biofilm removal by MZ-8 swarm and subsequent adherence of biofilm fragments (Scale bar, 1 μm.) (*C2*) SEM image of the spike-like surface structure of MZ-8 penetrating biofilm's EPS structure (white dashed line outlined MZ-8's spike; green dashed line outlined biofilm.) (Scale bar, 1 μm.) (*D1*) Different treatment with biofilms on culture dish including Untreated Biofilm, Static MZ-8 (Biofilm treated by static MZ-8 swarm), and Dynamic MZ-8 (Biofilm treated by dynamically moving MZ-8 swarm). (*D2*) Colony formation assay for assessing bacterial viability. (*E1* and *E2*) Crystal violet analysis. (*F1–F6*) BF images of MZ-8 movement on titanium plate for biofilm eradication. (Scale bar, 1.5 cm.) Crystal violet staining of titanium plate with biofilm (*G1*) and treated by MZ-8 (*G4*). SEM images of titanium plate with biofilm (*G2*) and treated by MZ-8 (*G5*). (*G3* and *G6*) Corresponding magnification of (*G2* and *G5*). (Scale bar, 10 μm.) (*G7*) Colony formation assay from (*G1* and *G4*). (*H1–H3*) Flow cytometry analysis of macrophage phenotypes in phosphate-buffered saline (PBS) group (macrophages cocultured with phosphate buffered saline solution), PGF group (macrophages cocultured with PGF), and MZ-8 group (macrophages cocultured with MZ-8 swarm) treatment groups. (*H4* and *H5*) Quantitative analysis of macrophage subpopulations based on flow cytometry. (*I*) Representative CLSM images of BMDM cells cultured on different samples (green: CD163; red: CD206; blue: nuclei.) (Scale bar, 25 μm.) (*J1–J3*) qPCR analysis of M2 macrophage polarization-related markers (YM1, CD206, IL-10).

movement—including dispersion, aggregation, and displacement—on culture dishes, effectively mechanically eradicating biofilms (Fig. 2 *A1–A6*). In addition, BF images of the eradicated biofilm in an "H" letter-shape demonstrated the precise controllability of MZ-8 swarm (Fig. 2*B*1 and *SI Appendix*, Fig. S11), and the efficiency of eradication was verified by fluorescence imaging (Fig. 2 *B2* and *B3*). As introduced previously, the spike-like morphology of MZ-8 was biomimetically designed for biofilm scraping Fig. 2*C*1). The detailed process of MZ-8 penetration was unveiled by SEM image (Fig. 3*C2* and *SI Appendix*, Fig. S12). The images revealed

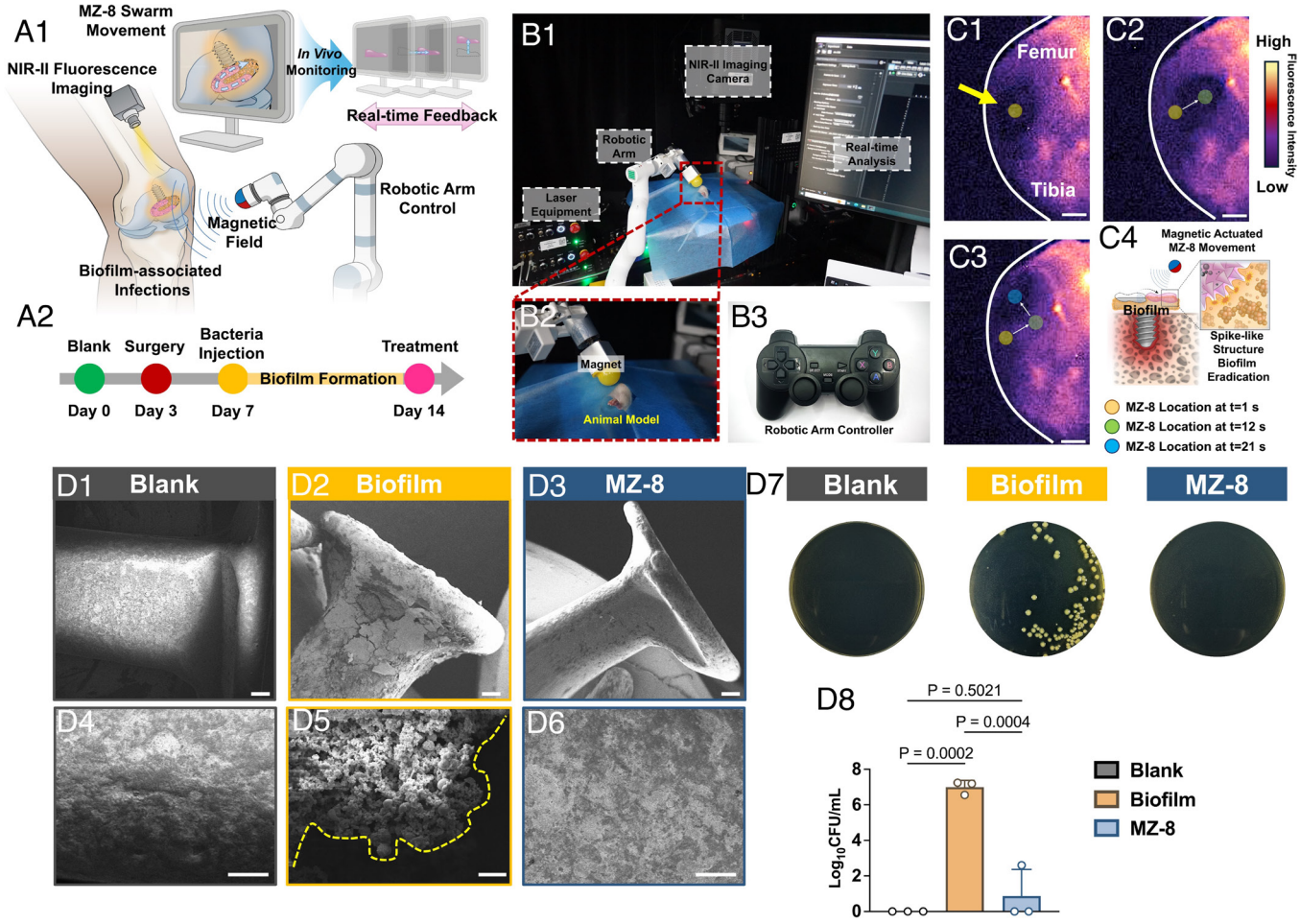

Fig. 3. In vivo biofilm eradication via MZ-8 in a rat PJI model. (*A1*) Schematic illustration of MZ-8 swarm-assisted biofilm eradication in a rat model with a joint implant. (*A2*) Schematic illustration of biofilm eradication treatment timeline. Real-time monitoring platform (*B1*) designed for living animal (*B2*) integrating robotic arm control (*B3*), magnetic actuation, and NIR-II fluorescence imaging for precise navigation and actuation of MZ-8 in vivo. (*C1*) In vivo real-time imaging monitoring of MZ-8 swarm (indicated by yellow arrow) after intra-articular injection for biofilm eradication treatment. (*C2* and *C3*) Illustrated MZ-8's movement (indicated by white arrows) across the joint implant surface. (Scale bar, 2 mm.) (*C4*) Schematic illustration of MZ-8's movement for biofilm eradication. (*D1*–*D3*) SEM analysis of joint implants under different treatments: Blank (Joint implant with no biofilm infection), Biofilm (Joint implant with biofilm infection), and MZ-8 (Joint implant with biofilm infection treated by MZ-8 swarm) (Scale bar, 200 μm), with (*D4*–*D6*) magnification of surface details (yellow dash line indicated biofilm, Scale bar, 100 μm, 2 μm, 100 μm.) (*D7* and *D8*) Colony culturing and quantification of biofilm eradication.

that the biomimetic spiny structures physically pierced through the biofilm matrix, suggesting that this mechanism effectively disassembles the matrix and exposes the embedded bacterial clusters. Quantitatively, compared to the Untreated Biofilm group and the Static MZ-8 group, the Dynamic MZ-8 group (Fig. 2*D1*) resulted in substantial biofilm eradication, which was confirmed by colony formation assay (Fig. 2*D2*) and crystal violet analysis (Fig. 2 *E1* and *E2*). Furthermore, robust antibacterial efficacy was consistently observed across other two types of biofilms formed by different strains (*Staphylococcus epidermidis* and *Escherichia coli*) (*SI Appendix*, Fig. S13 and S14), supporting highly efficient biofilm eradication achieved by MZ-8 swarm.

Subsequently, the antibiofilm activity of MZ-8 swarm was further verified on titanium plates, a material highly relevant to titanium implants. Under magnetic control, MZ-8 swarms effectively traversed the titanium surface and removed adhered biofilms via mechanical action (Fig. 2 *F1*–*F6*). Crystal violet staining and SEM imaging clearly demonstrated the biofilm elimination efficacy on titanium substrates. In the Untreated Biofilm group, dense and intact biofilms were observed through crystal violet staining (Fig. 2*G1*), SEM imaging (Fig. 2*G2*), and corresponding magnified views (Fig. 2*G3*). By contrast, after treatment with Dynamic MZ-8, titanium surfaces showed markedly reduced biofilm coverage, as evidenced by crystal violet staining (Fig. 2*G4*), SEM imaging (Fig. 2*G5*), and high-magnification images (Fig. 2*G6*). Consistent with these morphological observations, quantity of biofilm was significantly reduced in the dynamic MZ-8 treatment group (Fig. 2*G7*), corroborating the efficient eradication capability of MZ-8 swarm on metallic surfaces. Moreover, the broad-spectrum antibacterial effect against various strains (*S. epidermidis* and *E. coli*) was again confirmed in titanium plate assays, as supported by results in *SI Appendix*, Fig. S15.

Following the first stage of antibiofilm activity, the second stage involving Zn^{2+}-mediated immunomodulation was initiated. Zn^{2+} ions, released gradually during the degradation of the ZIF-8 framework, promoted macrophage polarization from a pro-inflammatory M1 phenotype toward a reparative M2 phenotype. Flow cytometry analysis revealed a significant increase in $CD206^{+}/CD86^{-}$ M2 macrophage populations, which were quantified in the Q3 quadrant (Fig. 2 *H1*–*H3*). Notably, the MZ-8 treatment group showed a marked shift toward the Q3 quadrant, in contrast to the predominantly M1 macrophages found in the PBS and PGF groups. Quantitative analysis confirmed a substantial rise in the proportion of M2 macrophages in the MZ-8 group (Fig. 2 *H4* and *H5*), underscoring the shift in macrophage polarization toward an anti-inflammatory M2 phenotype. Immunofluorescence staining

revealed that MZ-8 treatment significantly increased the expression of M2 markers, CD206 and CD163, in macrophages compared to the PBS and PGF groups (Fig. 2*I*). qPCR results further confirmed these findings. The MZ-8 group showed significantly higher expression of *YM1* (Fig. 2*J*1) and *CD206* (Fig. 2*J*2), both markers of M2 macrophages. Additionally, *IL-10* was also upregulated in the MZ-8 group (Fig. 2*J*3), indicating polarization toward the M2 phenotype. In addition, cell viability assays confirmed the excellent biocompatibility of MZ-8 with mesenchymal stem cells and human umbilical vein endothelial cells across all tested concentrations (*SI Appendix*, Fig. S16). In short, these results demonstrated that the MZ-8 swarm achieved sequential biofilm clearance and immune microenvironment modulation for comprehensive treatment of periprosthetic joint infection. To sum up, the two-step sequential therapeutic effects of MZ-8 were verified: i) magnetically actuated spiny swarms enabled efficient biofilm eradication at first, and ii) acid-responsive Zn^{2+} release from ZIF-8 coatings provided immunoregulatory cues to support subsequent tissue repair.

In Vivo Biofilm Eradication and Tissue Repair Via MZ-8 in a Rat Model. The therapeutic efficacy of MZ-8 swarm as a treatment was assessed in vivo using a rat femoral implant PJI model with biofilms (Fig. 4*A*1 and *SI Appendix*, Fig. S17). The biofilm eradication treatment timeline is shown in Fig. 4*A*2. To enable real-time monitoring of movement of the MZ-8 swarm within the body, second near-infrared (NIR-II) fluorescence imaging based on PbS-QDs as the NIR-II fluorescence fluorophores, was utilized and allowed precise real-time observation of MZ-8 swarm dynamics in vivo (*SI Appendix*, Figs. S18–S20). Thus, a monitoring platform (Fig. 4*B*1), integrating a robotic arm, rotating magnetic field, and NIR-II fluorescence imaging system, was established for precise delivery and navigation of MZ-8 swarm within the knee joint cavity (Fig. 4*B*2), utilizing robotic arm control (Fig. 4*B*3). Depending on this platform, MZ-8 swarms were tracked in real time in vitro and in vivo (*SI Appendix*, Figs. S21–S23 and Movies S2 and S3), showing precise intra-articular navigation in a valid PJI model.

First, the spiny-architectured MZ-8 swarm mechanically eradicated biofilms from the implant surface, guided by real-time in vivo imaging. After magnetically steered delivery into the infected knee, the collective motion driven by a rotating magnetic field, enabled the MZ-8 swarms to actively scrape biofilms from the surface of the implant, the real-time trajectory of which could be clearly seen (Fig. 4 *C*1–*C*3 and Movie S4). SEM images revealed an almost complete eradication of biofilms on MZ-8-treated implants (Fig. 4 *D*3 and *D*6), in stark contrast to the Blank group (Fig. 4 *D*1 and *D*4) and PGF group (Fig. 4 *D*2 and *D*5). Additionally, quantitative colony assays aligned with the SEM results, yielding 87.6% eradication efficiency (Fig. 4 *D*7 and *D*8). These findings demonstrated that magnetically actuated MZ-8 swarms, monitored in real time via NIR-II fluorescence imaging, constituted a highly effective in vivo anti-biofilm modality.

In summary, the spatiotemporal pattern of magnetically controlled MZ-8 swarm was successfully tracked in vivo using NIR-II fluorescence imaging in a rat model with biofilm-associated joint implant infection. MZ-8 treatment showed superior efficacy, effectively eradicating biofilms, exhibiting a favorable safety profile and decisive translational advantages as a complement to current biofilm treatment modalities.

Immunomodulation-Mediated Tissue Repair Via MZ-8 Treatment. Second, to decouple the immunomodulatory contribution of Zn^{2+} release, in vivo comparison among Biofilm, PGF, and MZ-8 groups confirmed that only MZ-8, via its pH-responsive function, robustly modulated the immune microenvironment and promoted tissue repair (*SI Appendix*, Fig. S24). The tissue repair process and underlying immunomodulation after MZ-8 treatment are illustrated in Fig. 3*A*. The MZ-8's precise placement within the joint cavity was monitored using real-time imaging, as shown in *SI Appendix*, Fig. S25, which displays the exact position of MZ-8 within the femur and tibia during treatment. At the end of the tissue repair treatment. Micro-CT images showed bone remodeling in the Biofilm, PGF, and MZ-8 (Fig. 3*B*1) groups. The MZ-8 group exhibited the most significant bone regeneration, with continuous bone bridging the defect. In contrast, the Biofilm group showed sparse bone formation, and the PGF group demonstrated partial bone ingrowth. Quantification of bone surface density (Fig. 3*B*2), percent bone volume, and trabecular number (*SI Appendix*, Fig. S26) showed a significantly higher trabecular count in the MZ-8 group compared to the Biofilm and PGF groups, indicating superior bone remodeling and regeneration in the MZ-8-treated group. Further comparison between the MZ-8 and PGF groups showed that MZ-8 treatment not only enhanced bone repair but also supported better overall recovery, evidenced by the improved weight recovery in the MZ-8 group (*SI Appendix*, Fig. S27), suggesting a more favorable healing response in the animals treated with MZ-8. Finally, biosafety assays confirmed that PbS-QDs and MZ-8 swarm were well tolerated, with no significant histological damage (*SI Appendix*, Fig. S28) or adverse changes in hematology, serum chemistry, or inflammatory markers (*SI Appendix*, Fig. S29). Thus, the in vivo platform successfully controlled MZ-8 swarm within the knee joint, enabling targeted Zn^{2+} release, demonstrating superior tissue repair.

To elucidate the specific process, immunofluorescence staining of the rat-model bone tissue (Biofilm, PGF, and MZ-8 groups) was performed, followed by quantitative comparison. The COL1A1 immunostaining revealed a pronounced elevation in collagen deposition, indicative of a densely elaborated extracellular matrix (Fig. 3 *C*1–*C*4). Concomitantly, the marked expansion of RUNX2-immunopositive cells in the MZ-8 group signified a robust acceleration of osteogenic lineage commitment and differentiation (Fig. 3 *D*1–*D*4). Then, transcriptomic analysis was performed across the three groups. The PCA revealed distinct clustering between the three groups, indicating notable differences in their transcriptional profiles (Fig. 3*E*). Moreover, the volcano plot analysis revealed that, in the MZ-8 group 622 genes were upregulated and 1229 genes downregulated compared with the Biofilm group (Fig. 3*F*), while 308 genes were upregulated and 1,201 downregulated compared with the PGF group (*SI Appendix*, Fig. S30). Thus, the results unveiled a pronounced, treatment-specific reprogramming of the transcriptional landscape following MZ-8 treatment. On this basis, GO enrichment analysis demonstrated that MZ-8 treatment evoked a significant transcriptional up-regulation of processes governing immune regulation and tissue repair, most prominently those implicated in extracellular-matrix organization, directed cell migration, and tissue remodeling (Fig. 3*G*). These findings were corroborated by GSEA, which independently confirmed a robust enrichment of immune-modulatory and pro-regenerative gene signatures after MZ-8 treatment with the "regulation of immune response" pathway exhibiting the most pronounced positive enrichment (Fig. 3*H*). Collectively, it was verified that MZ-8 treatment promoted tissue repair, plausibly via the potentiation of enhanced immunomodulation.

To further elucidate the immunomodulation induced by MZ-8 treatment in detail, M2 macrophage markers CD86, CD206, and CD163 were detected by immunostaining across the three groups

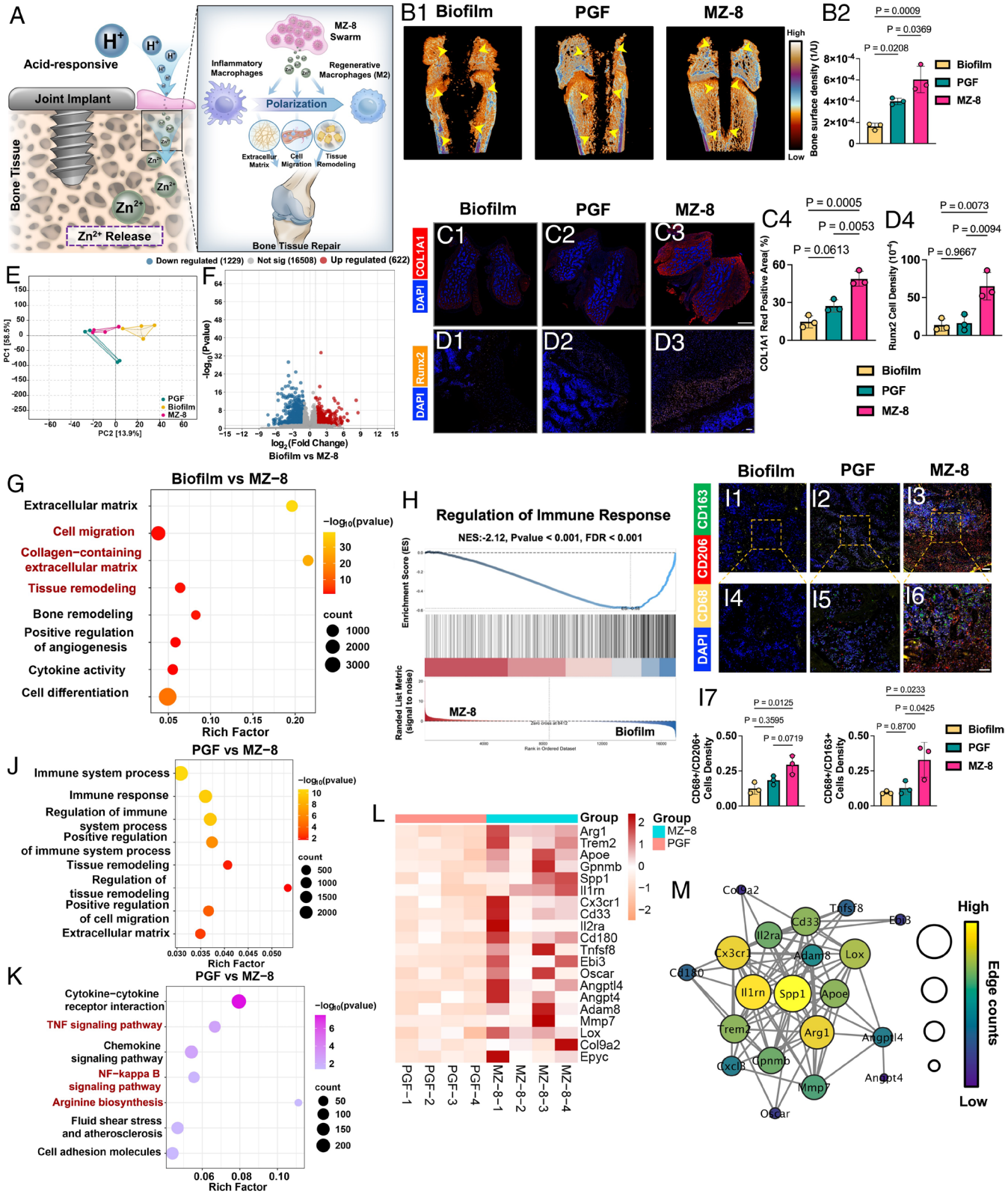

Fig. 4. Immunomodulation-mediated tissue repair via MZ-8 treatment. (*A*) Schematic illustration of tissue repair and immunomodulation induced by MZ-8 treatment. (*B1*) Micro-CT images showing bone remodeling across the three groups: Biofilm (Joint implant with biofilm infection), PGF (Joint implant with biofilm infection treated by PGF), and MZ-8 (Joint implant with biofilm infection treated by MZ-8 swarm) (Scale bar, 2 mm.), with corresponding quantifications of bone density (*B2*). (*C1*–*C3*) Immunofluorescence staining images of COL1A1 (Scale bar, 1 mm.) and (*D1*–*D3*) Runx2 (Scale bar, 100 μm.) across Biofilm, PGF, and MZ-8 groups. (*C4* and *D4*) Corresponding quantifications. (*E*) Principal component analysis (PCA) of Biofilm, PGF, and MZ-8 groups. (*F*) Volcano plots of differential gene expression of MZ-8 group vs Biofilm group (*G*) Gene Ontology (GO) enrichment analysis and (*H*) Gene Set Enrichment Analysis (GSEA) of MZ-8 group vs Biofilm group. (*I1*–*I3*) Immunofluorescence staining images of CD68/CD206/CD163 across Biofilm, PGF, and MZ-8 groups (Scale bar, 100 μm.) with (*I4*–*I6*) magnification (Scale bar, 20 μm.) (*I7*) Corresponding quantifications. (*J* and *K*) GO and Kyoto Encyclopedia of Genes and Genomes (KEGG) pathway enrichment analyses and (*L*) heatmap of representative upregulated genes of MZ-8 group vs PGF group. (*M*) Protein–protein interaction (PPI) network analysis of significantly regulated genes in the MZ-8 group.

(Fig. 3 *I*1–*I*7). Both $CD68^{+}CD206^{+}$ and $CD68^{+}CD163^{+}$ macrophages were significantly up-regulated in the MZ-8 group, suggesting that Zn^{2+} released from MZ-8 may drive macrophage polarization toward the reparative M2 phenotype. Transcriptomically, GO enrichment analysis between the MZ-8 and PGF groups revealed that MZ-8 significantly activated gene sets linked to immune system processes, cytokine–receptor interactions, and tissue remodeling (Fig. 3*J*). Concurrently, key KEGG pathways including TNF signaling, NF-κB signaling, and arginine biosynthesis, a pathway closely associated with M2 macrophage polarization, were significantly enriched (Fig. 3*K*). Together, it was indicated that MZ-8 treatment established a pro-repair environment by transcriptomically steering macrophages toward an M2 phenotype and simultaneously activating immune-modulatory pathways through Zn^{2+} release.

Additionally, a gene-level heat map further resolved that *Arg1*, *Il1rn*, *Spp1*, *Trem2*, and *Apoe* were selectively up-regulated in the MZ-8 group, corroborating robust immune-regulatory and pro-repair transcriptional activity (Fig. 3*L*). In addition to these key M2 macrophage polarization genes, other genes such as *Cx3cr1*, *Cd33*, *Adam8*, and *Lox* were also enriched. *Cx3cr1* and *Cd33* are involved in macrophage recruitment and tissue remodeling (24–27), while *Adam8* and *Lox* are associated with extracellular matrix remodeling and collagen synthesis (28, 29). Taken together, these genes jointly propagated the immune-modulatory and pro-regenerative program elicited by MZ-8 treatment. Notably, PPI network analysis revealed that *Arg1*, *Il1rn,* and *Spp1* were the central nodes in the gene network, suggesting they were critical regulators (Fig. 3*M*). These M2-related genes formed a tightly connected network, underscoring their key role in immunomodulation and tissue repair. In short, the crucial role of M2 polarization driven by Zn^{2+} release from MZ-8 was highlighted, further clarifying immunomodulation-mediated tissue repair orchestrated by MZ-8 treatment.

MZ-8 in a Rabbit Joint Implant Model and Human Knee Joint. Ultimately, the MZ-8 platform's clinical potential was mapped stepwise: efficacy and safety were additionally established in rabbits, and finally reproduced in human specimen, providing a coherent translational path from small-animal studies to preclinical human specimen evaluation. First, real-time NIR-II fluorescence imaging of magnetically driven MZ-8 swarms was successfully translated from mice to a rabbit knee-implant model. After standardized surgery (Fig. 5 *A*1–*A*4), the MZ-8 swarms exhibited steady, magnetic field-controlled locomotion throughout the larger joint cavity of rabbit (Fig. 5 *A*5 and *A*6), reproducing the spike-mediated scraping observed in rodents and confirming the first therapeutic step in a higher-order preclinical model. In addition, hematology,

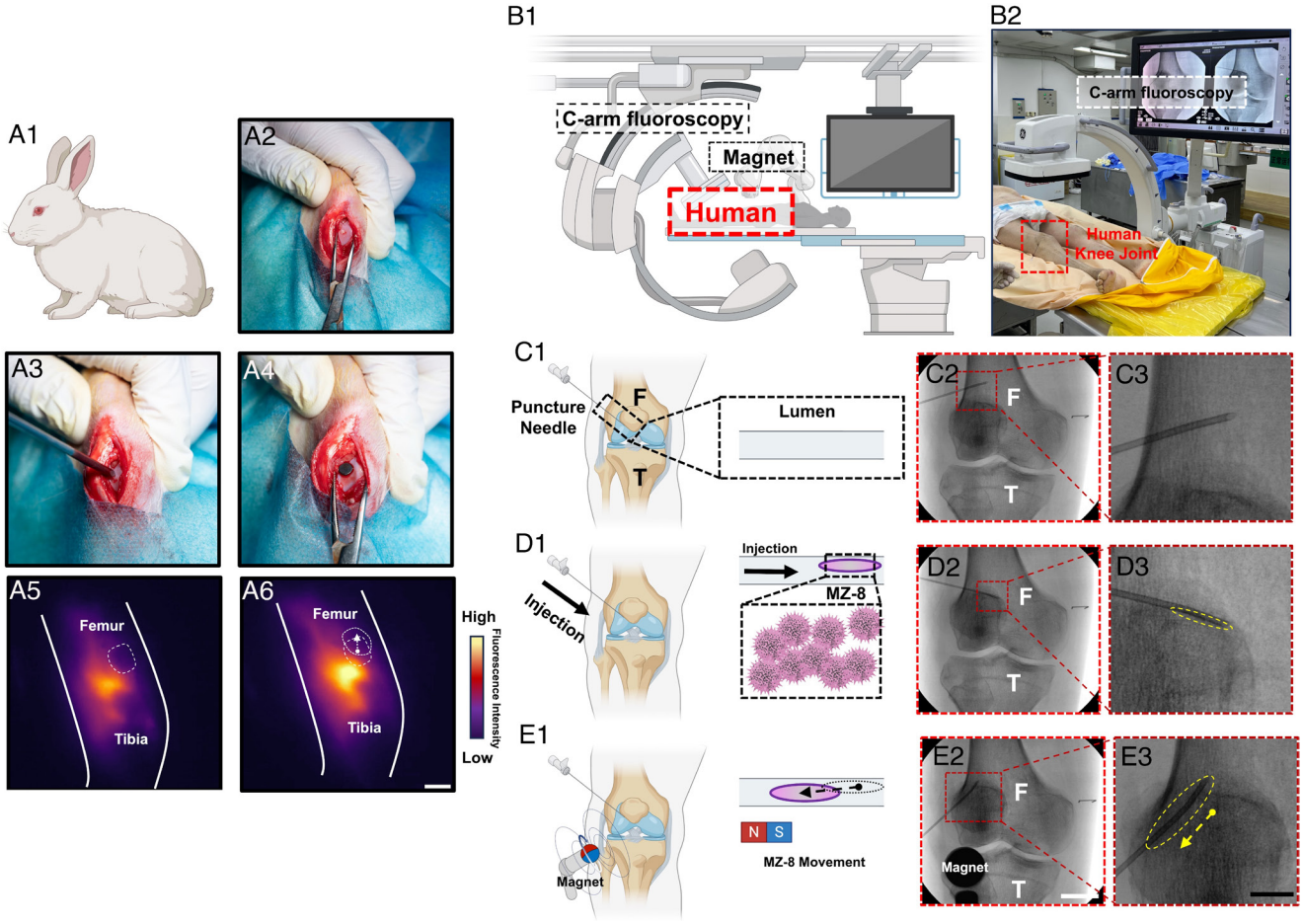

Fig. 5. MZ-8 in a rabbit joint implant model and human knee joint specimen. (*A*1–*A*4) Surgical procedure for establishing a rabbit knee-implant model. (*A*5 and *A*6) In vivo imaging of magnetic actuation and movement of MZ-8 in the rabbit knee joint. The white dashed circle indicated MZ-8; white arrows showed its trajectory. (Scale bar, 1 cm.) (*B*1) Clinical setup schematic for human specimen validation using C-arm fluoroscopy with magnetic field assistance. (*B*2) Photograph of the experimental setup including C-arm fluoroscopy and a human knee joint specimen. (*C*1–*C*3) Puncture needle and knee joint's schematic and corresponding fluoroscopic images. (*D*1–*D*3) Injection procedure of MZ-8 (yellow dashed circle). (*A*1, *B*1, *C*1, *D*1, and *E*1) are adapted from figure created in BioRender. H. Lee (2026) https://BioRender.com/kor84sm. (*E*1–*E*3) MZ-8's directional movement (yellow dashed circle) under magnetic control of MZ-8 (yellow dashed arrows) within the joint. [white (Scale bar, 3 cm.); black (Scale bar, 1 cm.)].

serum chemistry, and inflammatory markers showed no significant adverse effects (*SI Appendix*, Fig. S31), collectively demonstrating that the MZ-8 platform preserves targeted navigability, real-time monitorability, and an excellent safety profile when scaled to a large-animal anatomy with complexity.

Extending the translational pipeline, the MZ-8 swarms were tested in human cadaveric knee joints utilizing a clinical C-arm fluoroscope coupled to an external magnetic actuator (Fig. 5 *B*1 and *B*2). After needle injection, real-time radiographs revealed instantaneous, high-fidelity control of MZ-8 swarms' distribution and steering throughout the joint cavity (Fig. 5 *C*1–*C*3). Controlled aggregation and directed locomotion were reproducibly executed via the multifunctional platform (Fig. 5 *D*1–*D*3 and *E*1–*E*3). To sum up, the MZ-8 platform exhibited scalable controllability and therapeutic feasibility and could be navigated with standard operating-room equipment, providing a prospective pathway toward image-guided, precision treatment of biofilm-associated infections in clinical practice in future.

Discussion

In this study, we introduce the MZ-8 microrobotic system, a platform for treating biofilm associated-infections by integrating active mechanical biofilm ablation with targeted immunomodulation. Unlike passive delivery systems, MZ-8 embodies the essence of microrobots as interactive therapeutic carriers, enabling precise, image-guided execution. Our discussion highlights two key innovations: first, a two-step strategy combining biofilm eradication with tissue repair via Zn^{2+}-loaded ZIF-8, and second, the use of NIR-II fluorescence imaging and magnetic control for real-time, precision-guided navigation in complex biological environments.

In the first step—the battle against biofilm-associated infections—the active nature of microrobots offers distinct advantages over passive nanoparticles, which rely solely on uncontrolled drug release (30, 31), metal ion diffusion (32), or reactive oxygen species (ROS) generation (33). In contrast, microrobots can actively navigate, mechanically disrupt biofilms, and directly interact with bacterial colonies to enhance antimicrobial efficacy. Specifically, rotating magnetic fields generate torque that drives microrobots into rolling motion on surfaces (34–36), a mode that maximizes contact area with the biofilm for mechanical disruption (17, 37). While many recent studies have focused on optimizing microrobotic motion parameters to improve these effects (12, 13), our MZ-8 system integrates mechanical clearance with pathological microenvironment–responsive chemistry. Its core material, ZIF-8, belongs to the family of metal–organic frameworks (MOFs)—a class of crystalline, porous materials recently recognized by the 2025 Nobel Prize in Chemistry for their structural tunability and functional adaptability. The modular architecture of MOFs endows ZIF-8 with high surface area, adjustable pore environments, and intrinsic biodegradability (38, 39). More importantly, ZIF-8 is acid-labile (40, 41), enabling it to sense and respond to the acidic milieu characteristic of biofilm infection. This pH-triggered degradation synchronizes Zn^{2+} release precisely with biofilm disruption, achieving optimal kinetics within 10 to 30 min and transforming the microrobot from a passive carrier into an infection-responsive therapeutic actuator.

In the second step, Zn^{2+} ion release from MZ-8 promoted M2 macrophage polarization, as confirmed by flow cytometry, qPCR, and immunofluorescence. To explore the pro-healing mechanism, transcriptomic analysis revealed enriched signaling pathways, initiated by MZ-8 compared by PGF (no ZIF-8 coating), suggesting a three-phase healing process: inflammatory initiation, immune resolution, and tissue remodeling. We propose a model in which NF-κB and tumor necrosis factor (TNF) signaling orchestrates the initial phase of healing by triggering a controlled inflammatory response, which facilitates immune cell recruitment through the action of chemokines and cell adhesion molecules (CAMs) (42–44). Subsequently, the activation of the arginine biosynthesis pathway drives a pivotal transition toward inflammation resolution, potentially through promoting M2 macrophage polarization (45). This phenotypic shift underpins the transition from a pro-inflammatory environment to a pro-reparative one, facilitating efficient tissue repair. Moreover, key genes likely drive these phases: *Arg1* supports M2 polarization and phagocytosis, *Il1rn* modulates inflammation, and *Spp1* (osteopontin) promotes biomineralization and collagen stabilization during repair (46–48). This structured immunomodulatory response underscores MZ-8's therapeutic potential, seamlessly integrating biofilm clearance with regenerative healing. To further enhance its clinical applicability, the highly dynamic and often inaccessible environment of living tissues makes efficient navigation and real-time monitoring of MZ-8 paramount for validating its efficacy in vivo and enabling its eventual clinical translation. This critical need prompted our exploration of advanced imaging and control systems for the MZ-8 platform.

In biomedical robotics, imaging technologies are essential for advancing microrobot functionality and operational precision (18, 20). Conventional imaging modalities such as X-ray, MRI, PET, and optoacoustic tomography (OAT) often face a trade-off between resolution, real-time tracking, and minimally invasive operation (20). In contrast, NIR-II fluorescence imaging provides a noninvasive approach that minimizes light scattering and autofluorescence, thereby achieving superior tissue penetration and high spatial resolution for tracking MZ-8 microrobots in dynamic tissue environments (49, 50). Using real-time NIR-II fluorescence imaging, we visualized the spiral motion of the MZ-8 swarm between the femur and tibia, revealing its therapeutic trajectory within the joint cavity. Integrated with magnetic actuation, this closed-loop system allows precise navigation through narrow anatomical structures—including in vitro tubing, deep tissue cavities in rats and rabbits, and human specimens—supporting the clinical translation of real-time, precision-guided noninvasive interventions for treating biofilm-associated infections in orthopedic implants.

However, the current study has several limitations. While the rabbit model confirmed the basic safety and maneuverability of the MZ-8 system, the in vivo actuation parameters for effective biofilm clearance on surgical implants remain to be optimized. In addition, although NIR-II fluorescence imaging provides high-resolution visualization in preclinical settings, its clinical translation is currently constrained by ethical and regulatory barriers associated with optical imaging agents. Future work will focus on refining swarm control strategies for enhanced biofilm eradication and integrating clinically adoptable imaging modalities for real-time guidance in human applications.

In this study, the MZ-8 platform represents a closed-loop theranostic system that integrates real-time NIR-II imaging and magnetic actuation for precision treatment of biofilm-associated infections. By combining active mechanical biofilm disruption with microenvironment-responsive immunomodulation via Zn^{2+} release from its ZIF-8 coating, the system enables synergistic eradication of biofilms and reprogramming of the immune microenvironment. Beyond a single device, it embodies a therapeutic paradigm that merges precise magnetic navigation, real-time visual feedback, and a dual-action payload for synergistic intervention. This platform demonstrates the feasibility of microrobots as dynamically adjustable, human-supervised carriers capable of

performing, being monitored, and being fine-tuned in real time. With further development, this strategy holds significant potential to transform the treatment of biofilm-associated infections and other complex diseases where precision, adaptive intervention, and closed-loop control are crucial.

Materials and Methods

A detailed description of all experimental procedures is provided in *SI Appendix*. The following sections present a brief summary of the main methods employed in this study.

Microrobot Fabrication. Briefly, MZ-8 microrobots were synthesized using a pollen-templated method. Fe_3O_4 nanoparticles were deposited onto spiny PGs via in situ coprecipitation to impart magnetic responsiveness, followed by ALD-assisted ZIF-8 coating for pH-responsive Zn^{2+} release.

In Vitro Biofilm Eradication and Immunomodulation. Biofilms of *Staphylococcus aureus*, *S. epidermidis*, and *E. coli* were cultured on polystyrene plates and titanium surfaces. MZ-8 swarms were actuated under a rotating magnetic field, and biofilm eradication was assessed by colony-forming unit (CFU) counts, crystal violet staining, live/dead fluorescence imaging, and SEM. Immunomodulatory effects were evaluated by flow cytometry, immunofluorescence, and qPCR in RAW264.7 macrophages.

In Vivo Animal Models. A rat PJI model was established by implanting titanium implants into the distal femur and inoculating *S. aureus* into the joint cavity. A rabbit model was used for MZ-8 swarm navigation without bacterial inoculation. All animal experiments were approved by the Animal Care Committee of Fudan University.

Magnetic Actuation and Imaging. Briefly, magnetic actuation was performed using a rotating magnetic field generated by a robotic arm-controlled permanent magnet. Real-time tracking of MZ-8 swarms was achieved using a NIR-II fluorescence imaging system and a C-arm fluoroscope. Spatial and temporal resolution details are provided in *SI Appendix*.

In Vivo Biofilm Eradication and Tissue Repair. In the rat PJI model, MZ-8 swarms were delivered intra-articularly under NIR-II guidance and actuated for mechanical biofilm disruption. Biofilm eradication was quantified by CFU counts and SEM. Bone tissue was assessed by micro-CT, histology (H and E, Masson, Giemsa), immunofluorescence (CD68, CD206, CD163, COL1A1, Runx2), and transcriptomic analysis.

Human Cadaveric Study. Fresh-prepared human cadaveric knee specimens were used to evaluate the in-body magnetic manipulation of MZ-8 swarms under clinical C-arm fluoroscopic guidance. The human cadaveric study was approved by the Ethics Committee of RED CROSS society of China, Shanghai branch.

Statistical Analysis. Data are presented as mean ± SD. Statistical significance was determined by one-way ANOVA, two-way ANOVA, or a two-tailed unpaired Student's *t* test as appropriate, with $P < 0.05$ considered statistically significant.

Data, Materials, and Software Availability. The transcriptomic datasets used in this study have been deposited in the OMIX database and are accessible for review at: https://ngdc.cncb.ac.cn/omix/release/OMIX017811 (Accession: OMIX017811) (51).

ACKNOWLEDGMENTS. This work was supported by National Natural Science Foundation of China (82302787, 92580128 and 525B1002); Science and Technology Commission of Shanghai Municipality (23ZR1445700 and 24520750200); Medical Engineering Joint Fund of Fudan University (yg2023-29); Young Elite Scientists Sponsorship Program by CAST (2023QNRC001); Shanghai Chenguang Program (24CGA08); Shanghai "Rising Stars of Medical Talents" Youth Development Program (Youth Medical Talents–Specialist Program) and Youth Academy Incubation Program of Huashan Hospital (3030404002). The authors extend their gratitude to Prof. Yi Feng (Department of Integrative Medicine and Neurobiology, Fudan University) for her guidance on imaging equipment optimization. We also thank Sitong Li (School of Tropical Agriculture and Forestry, Hainan University) for her expert advice on marine biomimetic concepts, and Prof. You Liang and Oliver Manuel (Department of Mathematics, Toronto Metropolitan University) for their valuable input in in vivo video processing.

Author affiliations: [a]Sports Medicine Institute of Fudan University, Department of Sports Medicine, Huashan Hospital, Fudan University, Shanghai 200040, People's Republic of China; [b]International Institute for Intelligent Nanorobots and Nanosystems, College of Intelligent Robotics and Advanced Manufacturing, Fudan University, Shanghai 200433, People's Republic of China; [c]Zhejiang Key Laboratory of Extreme Environment Functional Materials, Yiwu Research Institute of Fudan University, Yiwu, Zhejiang 322000, People's Republic of China; [d]College of Computer Science and Artificial Intelligence, Fudan University, Shanghai 200433, People's Republic of China; [e]Institute of Natural Sciences, Shanghai Jiaotong University, Shanghai 200240, People's Republic of China; [f]Department of Anatomy and Physiology, Shanghai Jiao Tong University School of Medicine, Shanghai 200025, People's Republic of China; [g]School of Basic Medical Science, Fudan University, Shanghai 200032, People's Republic of China; [h]School of Medicine, The Chinese University of Hong Kong (Shenzhen), Shenzhen 518172, People's Republic of China; [i]International Institute for Intelligent Nanorobots and Nanosystems, College of Intelligent Robotics and Advanced Manufacturing, State Key Laboratory of Surface Physics, and State Key Laboratory of Photovoltaic Science and Technology, Fudan University, Shanghai 200433, People's Republic of China; and [j]Shanghai Frontiers Science Research Base of Intelligent Optoelectronics and Perception, Institute of Optoelectronics, Fudan University, Shanghai 200438, People's Republic of China

Author contributions: S.L., Yu Mei, Yongfeng Mei, J.C., G.H., and S.F. designed research; S.L., Yu Mei, K.X., H.S., B.X., B.J., C.Y., H.L., S.Z., X.Z., and Yueming Wang performed research; S.L., Yu Mei, K.X., Y.-a.C., M.T., B.X., B.J., Yi Wang, Y.Z., Z.L., and S.S. analyzed data; Y.-a.C. from the International Institute for Intelligent Nanorobots and Nanosystems of Fudan University conducted the finite element simulation analyses; M.T. from the College of Computer Science and Artificial Intelligence of Fudan University conducted the finite element simulation analyses; Yi Wang from the College of Computer Science and Artificial Intelligence of Fudan University performed the experiments on microrobot locomotion in in vitro environment; and S.L., B.J., H.L., Y. Wo, Z.L., S.S., Y.L., M.T., J.C., and G.H. wrote the paper.

1. P. Lampertico *et al.*, EASL 2017 clinical practice guidelines on the management of hepatitis B virus infection. *J. Hepatol.* **67**, 370–398 (2017).
2. S. Y. C. Tong, J. S. Davis, E. Eichenberger, T. L. Holland, V. G. Fowler, Staphylococcus aureus infections: Epidemiology, pathophysiology, clinical manifestations, and management. *Clin. Microbiol. Rev.* **28**, 603–661 (2015).
3. W. J. Wiersinga, A. Rhodes, A. C. Cheng, S. J. Peacock, H. C. Prescott, Pathophysiology, transmission, diagnosis, and treatment of coronavirus disease 2019 (COVID-19): A review. *JAMA* **324**, 782 (2020).
4. S. Zhang *et al.*, Immunomodulatory biomaterials against bacterial infections: Progress, challenges, and future perspectives. *Innovation* **4**, 100503 (2023).
5. C. Geng *et al.*, Achieving clearance of drug-resistant bacterial infection and rapid cutaneous wound regeneration using an ROS-balancing-engineered heterojunction. *Adv. Mater.* **36**, e2310599 (2024).
6. E. A. Masters *et al.*, Skeletal infections: Microbial pathogenesis, immunity and clinical management. *Nat. Rev. Microbiol.* **20**, 385–400 (2022).
7. H. C. Flemming *et al.*, The biofilm matrix: Multitasking in a shared space. *Nat. Rev. Microbiol.* **21**, 70–86 (2023).
8. K. Sauer *et al.*, The biofilm life cycle: Expanding the conceptual model of biofilm formation. *Nat. Rev. Microbiol.* **20**, 608–620 (2022).
9. S. R. Dabbagh *et al.*, 3D-printed microrobots from design to translation. *Nat. Commun.* **13**, 1–24 (2022).
10. P. Fischer, B. J. Nelson, Tiny robots make big advances. *Sci. Robot.* **6**, eabh3168 (2021).
11. Y. Dong *et al.*, Endoscope-assisted magnetic helical micromachine delivery for biofilm eradication in tympanostomy tube. *Sci. Adv.* **8**, eabq8573 (2022).
12. B. Sun *et al.*, Liquid-bodied antibiofilm robot with switchable viscoelastic response for biofilm eradication on complex surface topographies. *Sci. Adv.* **11**, eadt8213 (2025).
13. G. Hwang *et al.*, Catalytic antimicrobial robots for biofilm eradication. *Sci. Robot.* **4**, eaaw2388 (2019).
14. Y. Fan *et al.*, Biomimetic piezoelectric nanomaterial-modified oral microrobots for targeted catalytic and immunotherapy of colorectal cancer. *Sci. Adv.* **10**, eadm9561 (2024).
15. S. Wang *et al.*, Magnetic soft microrobots for erectile dysfunction therapy. *Proc. Natl. Acad. Sci. U.S.A.* **121**, e2407809121 (2024).
16. G. Go *et al.*, Human adipose-derived mesenchymal stem cell-based medical microrobot system for knee cartilage regeneration in vivo. *Sci. Robot.* **5**, eaay6626 (2020).
17. M. Sun *et al.*, Magnetic microswarm and fluoroscopy-guided platform for biofilm eradication in biliary stents. *Adv. Mater.* **34**, e2201888 (2022).
18. B. Sun, S. Kjelleberg, J. J. Y. Sung, L. Zhang, Micro- and nanorobots for biofilm eradication. *Nat. Rev. Bioeng.* **2**, 367–369 (2024).
19. B. J. Nelson, S. Pané, Delivering drugs with microrobots. *Science* **382**, 1120–1122 (2023).
20. P. Wrede *et al.*, Synergistic integration of materials in medical microrobots for advanced imaging and actuation. *Nat. Rev. Mater.* **10**, 888–906 (2025).
21. L. Formery *et al.*, Molecular evidence of anteroposterior patterning in adult echinoderms. *Nature* **623**, 555–561 (2023).
22. E. Hebert, M. Silvia, G. M. Wessel, Structural and molecular distinctions of primary and secondary spines in the sea urchin Lytechinus variegatus. *Sci. Rep.* **14**, 1–13 (2024).
23. J. S. Pearse, Ecological role of purple sea urchins. *Science* **314**, 940–941 (2006).
24. G. S. Laszlo *et al.*, Expression and functional characterization of CD33 transcript variants in human acute myeloid leukemia. *Oncotarget* **7**, 43281–43294 (2016).

25. M. Lee, Y. Lee, J. Song, J. Lee, S. Y. Chang, Tissue-specific role of CX(3)CR1 expressing immune cells and their relationships with human disease. *Immune Netw.* **18**, e5 (2018).
26. Z. Qian *et al.*, Blockade of the ADAM8-Fra-1 complex attenuates neuroinflammation by suppressing the Map3k4/MAPKs axis after spinal cord injury. *Cell. Mol. Biol. Lett.* **29**, 75 (2024).
27. R. Laczko, K. Csiszar, Lysyl oxidase (LOX): Functional contributions to signaling pathways. *Biomolecules* **10**, 1093 (2020).
28. C. Bonnans, J. Chou, Z. Werb, Remodelling the extracellular matrix in development and disease. *Nat. Rev. Mol. Cell Biol.* **15**, 786–801 (2014).
29. J. Winkler, A. Abisoye-Ogunniyan, K. J. Metcalf, Z. Werb, Concepts of extracellular matrix remodelling in tumour progression and metastasis. *Nat. Commun.* **11**, 1–19 (2020).
30. H. Hu *et al.*, Hybrid biomimetic membrane coated particles-mediated bacterial ferroptosis for acute MRSA pneumonia. *ACS Nano* **17**, 11692–11712 (2023).
31. Y. Liu, Y. Li, L. Shi, Controlled drug delivery systems in eradicating bacterial biofilm-associated infections. *J. Control Release* **329**, 1102–1116 (2021).
32. J. Zhou *et al.*, Photothermal iron-based riboflavin microneedles for the treatment of bacterial keratitis via ion therapy and immunomodulation. *Adv. Healthc Mater.* **13**, e2304448 (2024).
33. Y. Zhao *et al.*, H(2)O(2) self-supplying and GSH-depleting nanosystem for amplified NIR mediated-chemodynamic therapy of MRSA biofilm-associated infections. *J. Nanobiotechnol.* **22**, 117 (2024).
34. H. Zhou, C. C. Mayorga-Martinez, S. Pané, L. Zhang, M. Pumera, Magnetically driven micro and nanorobots. *Chem. Rev.* **121**, 4999–5041 (2021).
35. I. S. M. Khalil, L. Abelmann, S. Misra, Magnetic-based motion control of paramagnetic microparticles with disturbance compensation. *IEEE Trans. Magn.* **50**, 1–10 (2014).
36. L. Yang, L. Zhang, Motion control in magnetic microrobotics: from individual and multiple robots to swarms. *Annu. Rev. Control Robot. Auton. Syst.* **4**, 509–534 (2021).
37. B. Sun *et al.*, Liquid-bodied antibiofilm robot with switchable viscoelastic response for biofilm eradication on complex surface topographies. *Sci. Adv.* **11**, eadt8213 (2025).
38. K. S. Park *et al.*, Exceptional chemical and thermal stability of zeolitic imidazolate fra meworks. *Proc. Natl. Acad. Sci. U.S.A.* **103**, 10186–10191 (2006).
39. R. Banerjee *et al.*, High-throughput synthesis of zeolitic imidazolate frameworks and application to CO_2 capture. *Science* **319**, 939–943 (2008).
40. A. Ganesan, J. Leisen, R. Thyagarajan, D. S. Sholl, S. Nair, Hierarchical ZIF-8 materials via acid gas-induced defect sites: Synthesis, characterization, and functional properties. *ACS Appl. Mater. Interfaces* **15**, 40623–40632 (2023).
41. Q. Wang, Y. Sun, S. Li, P. Zhang, Q. Yao, Synthesis and modification of ZIF-8 and its application in drug delivery and tumor therapy. *RSC Adv.* **10**, 37600–37620 (2020).
42. S. Chen *et al.*, Macrophages in immunoregulation and therapeutics. *Signal Transduct. Target. Ther.* **8**, 1–35 (2023).
43. A.-C. Feng *et al.*, The transcription factor NF-κB orchestrates nucleosome remodeling during the primary response to Toll-like receptor 4 signaling. *Immunity* **57**, 462–477.e469 (2024).
44. N. Parameswaran, S. Patial, Tumor necrosis factor-α signaling in macrophages. *Crit. Rev. Eukaryot. Gene Expr.* **20**, 87–103 (2010).
45. V. Bronte, P. Zanovello, Regulation of immune responses by L-arginine metabolism. *Nat. Rev. Immunol.* **5**, 641–654 (2005).
46. B. Depalle *et al.*, Osteopontin regulates type I collagen fibril formation in bone tissue. *Acta Biomater.* **120**, 194–202 (2021).
47. U. Jaggi *et al.*, Increased phagocytosis in the presence of enhanced M2-like macrophage responses correlates with increased primary and latent HSV-1 infection. *PLoS Pathog.* **16**, e1008971 (2020).
48. M. Attur *et al.*, Interleukin-1 receptor antagonist gene (IL1RN) variants modulate the cytokine release syndrome and mortality of COVID-19. *J. Infect. Dis.* **229**, 1740–1749 (2024).
49. Z. Hu *et al.*, First-in-human liver-tumour surgery guided by multispectral fluorescence imaging in the visible and near-infrared-I/II windows. *Nat. Biomed. Eng.* **4**, 259–271 (2020).
50. G. Pitruzzello, Seeing into deep tissue. *Nat. Photonics* **17**, 376–377 (2023).
51. S. Li, Data from "Transcriptomic analysis of periprosthetic infected femoral bone tissues in rats subjected to various treatments." OMIX database. https://ngdc.cncb.ac.cn/omix/release/OMIX017811. Deposited 17 June 2026.